Journal of Remote Sensing
A SCIENCE PARTNER JOURNAL

RESEARCH ARTICLE

Revolutionizing Clear-Sky Humidity Profile Retrieval with Multi-Angle-Aware Networks for Ground-Based Microwave Radiometers

Yinshan Yang[1], Zhanqing Li[2], Jianping Guo[3], Yuying Wang[4], Hao Wu[5], Yi Shang[4], Ye Wang[1], Langfeng Zhu[5], and Xing Yan[1*]

[1]Advanced Interdisciplinary Institute of Satellite Applications, Faculty of Geographical Science, Beijing Normal University, Beijing 100875, China. [2]Department of Atmospheric and Oceanic Sciences, Earth System Science Interdisciplinary Center, College Park, MD 21029, USA. [3]State Key Laboratory of Severe Weather, Chinese Academy of Meteorological Sciences, Beijing 100081, China. [4]Key Laboratory for Aerosol-Cloud-Precipitation of China Meteorological Administration, Nanjing University of Information Science & Technology, Nanjing 210044, China. [5]China Meteorological Administration Key Laboratory of Atmospheric Sounding, School of Electrical Engineering, Chengdu University of Information Technology, Chengdu 610225, China.

*Address correspondence to: yanxing@bnu.edu.cn

Citation: Yang Y, Li Z, Guo J, Wang Y, Wu H, Shang Y, Wang Y, Zhu L, Yan X. Revolutionizing Clear-Sky Humidity Profile Retrieval with Multi-Angle-Aware Networks for Ground-Based Microwave Radiometers. *J. Remote Sens.* 2025;5:Article 0736. https://doi.org/10.34133/remotesensing.0736

Submitted 4 February 2025
Revised 26 June 2025
Accepted 27 June 2025
Published 7 August 2025

Accurate retrieval of atmospheric relative humidity (RH) profiles is essential for improving our understanding of atmospheric thermodynamics and climate change. Nevertheless, it remains challenging, as traditional models rely exclusively on vertical brightness temperature (BT) observations. Here, we present a novel retrieval algorithm called AngleNet, a groundbreaking deep-learning model that leverages multi-angle BT observation from ground-based microwave radiometers (MWRs). The innovative "multi-angle-aware" module in AngleNet effectively exploits previously underutilized oblique scanning angle data by accurately capturing these nonlinear relationships between BT and RH profiles, and precisely characterizes its vertical fine structure. Based on the 7-year (2018–2024) in situ measurements from Beijing, Nanjing, and Shanghai, validation results reveal that AngleNet achieves substantial improvements, with an average R^2 of 0.71 and a root mean square error (RMSE) of 10.39%, surpassing conventional models such as LGBM (light gradient boosting machine) and RF (random forest) by over 10% in both metrics, and demonstrating a remarkable 41% increase in R^2 and a 10% reduction in RMSE compared to the previous BRNN method (batch normalization and robust neural network). Moreover, additional independent validation results demonstrate that AngleNet exhibits excellent stability and retrieval accuracy during periods without radiosonde measurements. Feature analysis and evaluations of the "multi-angle-aware" module indicate that optimal RH retrieval performance is achieved by combining zenith-angle BTs with oblique angles at 30° and 19.2°. AngleNet breakthrough performance is especially notable in consistently capturing complex RH profile features, which are critical for accurate numerical weather forecasting and climate monitoring.

Introduction

Accurately retrieving humidity profiles is crucial for capturing the vertical thermodynamic structure of the atmosphere, especially in the lowest few kilometers, which plays a vital role in weather forecasting and climate system analysis [1,2]. These profiles are essential for validating numerical weather prediction models and support a wide range of applications, including extreme weather forecasting, pollutant tracking, renewable energy optimization, and urban planning [1,3–5]. Microwave radiometers (MWRs) are passive microwave remote sensing instruments that receive microwave radiation emitted, scattered, or reflected by objects within the antenna's field of view. This radiation is converted into an equivalent blackbody temperature, from which temperature and humidity profiles are subsequently retrieved [6,7]. A key advantage of MWRs is their ability to provide continuous, high-temporal-resolution measurements in the boundary layer and lower troposphere, enabling effective observation of atmospheric evolution processes and partially mitigating the limitations of radiosonde networks and satellite-based remote sensing [8–10]. Therefore, various MWRs are extensively deployed at meteorological observation stations worldwide. Their reliability and accuracy have been widely demonstrated through long-term operations across mid-latitude, tropical, and polar regions [11–14].

Operational MWR networks are being progressively established worldwide, with a substantial increase in deployments expected in the near future [10,15]. Notable initiatives include the Atmospheric Radiation Measurement (ARM) Program in the

United States [13], the Mesonet in the state of New York [16], as well as European networks such as E-PROFILE and CLIWA-NET [17–19]. Additionally, the Urban Meteorological Observation System in Seoul, South Korea [20], and a network of over 100 MWRs across China further exemplify global efforts to enhance atmospheric monitoring. Despite the remarkable advancements in observational instruments and inversion algorithms, challenges persist in achieving accurate retrieving humidity profiles. This is largely due to the complex, nonlinear relationship between humidity and brightness temperature (BT) across various spectral frequencies, compounded by the limited sensitivity of individual frequency bands to water vapor and oxygen [21,22].

The retrieval of atmospheric humidity profiles from multi-wavelength BT data from MWRs remains a central challenge. Recent advancements in retrieval algorithms have primarily relied on 3 approaches: statistical regression, physical iterative methods, and machine learning [3,22–26]. Statistical regression methods, such as linear and quadratic approaches, are efficient but limited by their reliance on linear relationships, which fail to capture the complex, nonlinear interactions between BT and atmospheric profiles, particularly under varying atmospheric conditions [23,25]. Physical approaches, like the optimal estimation (OE) technique, combine MWR data with prior knowledge to iteratively refine humidity estimates [23]. However, these methods are computationally demanding and sensitive to assumptions about model accuracy, making them less suitable for real-time applications [22,24].

While physical methods have made use of multi-angle BT data, their accuracies in relative humidity (RH) retrieval remain constrained by a limited understanding of the relationship between RH profiles and multi-angle BT [3,21,22,26–30]. In contrast, machine learning approaches, particularly deep learning models, have gained attention for their ability to extract complex relationships from data through multi-layered neural networks. These methods offer important promise for retrieving atmospheric temperature and humidity profiles by extracting complex, nonlinear features from BT data [26,31–36]. However, a critical gap remains in current machine learning-based methods: They typically focus on MWR vertical signal data, disregarding valuable information across multiple elevation scanning angles beyond the vertical. This limitation overlooks the potential of multi-angle BT data, which could provide richer and more accurate insights into atmospheric profiles, especially for humidity retrieval.

To address these challenges, this study develops a novel deep learning model, the multi-angle-aware network (AngleNet), specifically designed to exploit BT signals from all channels at multi-angle captured by ground-based MWR. AngleNet integrates BT from multiple angles, moving beyond the conventional emphasis on vertical signals. By integrating multi-angle information, AngleNet facilitates a more comprehensive analysis of atmospheric humidity profiles, capturing the complex nonlinear relationships between BT and humidity across diverse atmospheric conditions. This approach represents a substantial advancement in retrieval accuracy and robustness, enhancing the model's capability to address the intrinsic challenges of retrieving humidity profiles in the atmospheric field.

Materials and Methods

To leverage the latent information from MWR channels with unused elevation scanning angles, we propose AngleNet. Initially, we assessed the data quality from MWRs, radiosondes, and millimeter-wavelength cloud radars (MWCRs) [37–40]. Next, we synchronized the height and time conditions for profiles from these instruments and integrated them with ERA5 reanalysis data [41] to identify clear-sky samples more effectively and mitigate cloud interference. Prior to model training, rigorous preprocessing of each dataset was implemented. Radiosonde RH profiles served as the dependent variable, while ERA5 RH profiles filled temporal gaps [outside of 08:00 and 20:00 local standard time (LST)]. Radiosondes served as the reference standard, and the ERA5 RH profiles were quality-controlled (QC) following the methodology described in [33]. BTs from 8 scanning angles (ranging from vertical to 5° above the horizon) were used, collected from MWR sites with unobstructed views [22,29]. Surface meteorological data (e.g., pressure, temperature, and RH) were included as independent variables, representing global features in AngleNet. Angle-specific BT data were treated as angle-aware variables (local features), along with additional categorical variables such as location, month, and hour. After preprocessing, the data were fed into AngleNet, along with conventional deep learning models like light gradient boosting machine (LGBM) and random forest (RF), as well as the original MWR products for comparative evaluation. A 5-fold cross-validation (CV) method was employed for model training and hyperparameter optimization. Finally, independent validation was conducted using encrypted radiosonde data from Nanjing and Shanghai, collected outside regular observation periods.

Data

Location and datasets

This study combines ground-based MWR and radiosonde data collected in Beijing, Nanjing, and Shanghai from 2018 to 2024, along with MWCR and QC ERA5 reanalysis data, to tackle the challenges posed by cloud interference and temporal gaps in radiosonde observations. The goal is to enhance the retrieval accuracy of RH profiles. A total of 8,667 QC RH profiles were used in this analysis. The specific observational periods, instrumentation, location details, and sample sizes for the comprehensive long-term field experiments conducted in each city are provided in Fig. 1 and Table S1. For sites where radiosonde and MWR observations were not colocated, additional MWCR data were incorporated at the MWR observations to mitigate cloud effects. A detailed description of the instruments used in this study is provided in Text S1.

Figure 1 provides the distribution and topography of the 3 cities involved in the study. The Beijing site (Fig. 1A and F) is located at the Beijing Meteorological Observatory, which is surrounded by the Fifth Ring Road (semi-highway), industrial parks, and residential areas [42,43]. The Nanjing MWR site (Fig. 1B and C), situated at Nanjing University of Information Science & Technology, is paired with radiosonde data from the Jiangning station, located approximately 35 km away [43,44]. The Shanghai MWR site (Fig. 1D and E) was initially located at Baoshan Meteorological Observatory and later relocated to Fudan University, both situated in areas surrounded by residential neighborhoods. For both Nanjing and Shanghai, despite the slight spatial separation between the MWR and radiosonde sites, the similar underlying surface conditions and minimal topographical barriers ensure a high degree of consistency between MWR and radiosonde data, making these sites suitable for training the deep learning algorithms used in this study. Figure 1G and H illustrates the temporal distribution of RH

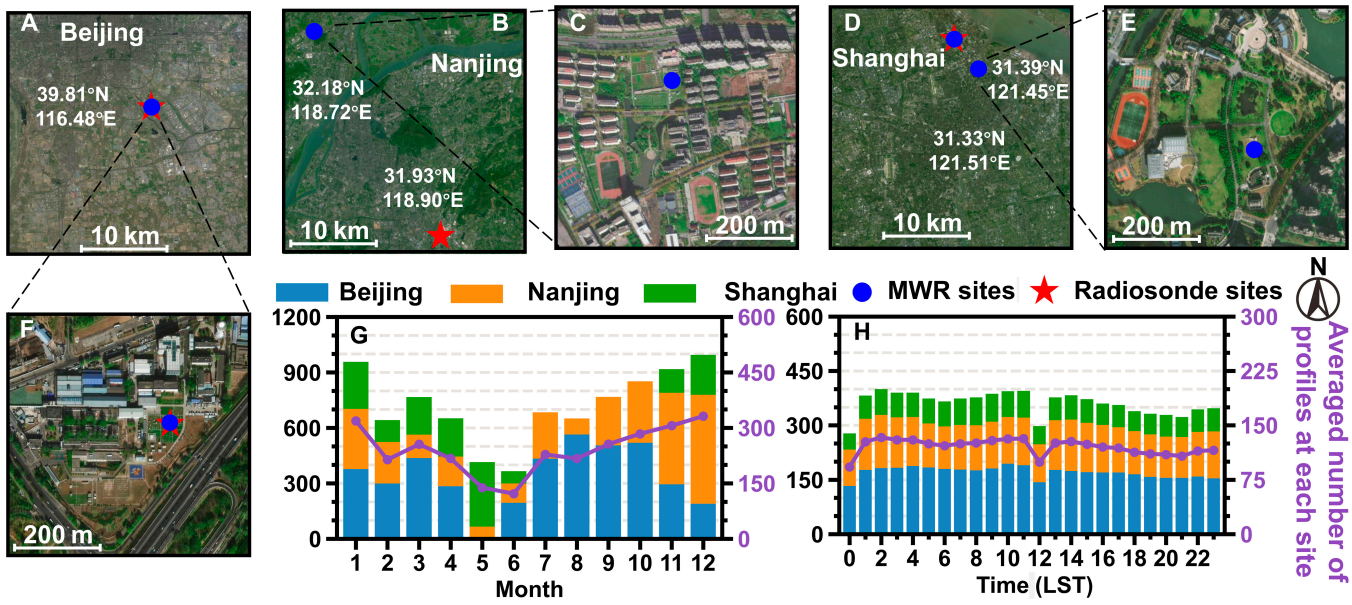

Fig. 1. Distribution of the deployments of instruments used in this study and images of their surroundings in Beijing (A and F), Nanjing (B and C), and Shanghai (D and E). Blue dots represent locations of MWRs, while red dots denote radiosonde sites. The total number of profiles (left *y* axis, bars, colors represent different cities) per month or hour (G and H) and the average number of profiles per site (right *y* axis, purple dots and lines).

profiles across the study period. The number of profiles per month peaks in the autumn and winter months, reflecting the lower frequency of cloudy and rainy days, with over 900 profiles recorded in January and December. The hourly distribution remains fairly stable, with 250 to 400 profiles recorded per hour, ensuring balanced data coverage throughout the day. Profiles at 08:00 and 20:00 LST are directly aligned with radiosonde data, while profiles at other times are supplemented by QC ERA5 data, effectively filling in the temporal gaps in radiosonde observations.

Data preprocessing

Measurements from the MWR, MWCR, and radiosonde were rigorously quality-checked [45–47]. Outliers were detected and removed using cubic spline interpolation, and all profiles were standardized to a vertical resolution of 115 layers (0 to 10 km), as detailed in Text S2. To minimize systematic errors, instruments should collect data simultaneously at colocated sites. However, slight spatial discrepancies between instruments in Nanjing and Shanghai were unavoidable due to experimental constraints. Specifically, the MWR and radiosonde sites are separated by approximately 35 km in Nanjing and about 8 km in Shanghai, while MWCR is always colocated with the MWR. To account for these discrepancies, measurements from MWCR and onboard rain sensors of the MWR were employed to evaluate weather conditions at MWR site. Only data recorded under clear-sky conditions at both the MWR and radiosonde sites simultaneously were retained.

To further mitigate spatial discrepancies caused by noncolocation or radiosonde drift, ERA5 cloud cover and RH profiles—averaged over a 3×3 grid—were incorporated. In addition to retrieving profiles from the MWR using radiosonde data, climatological datasets such as QC ERA5 were used when radiosonde data were unavailable [22,33]. Previous studies have demonstrated that integrating ERA5 data with radiosonde observations substantially improves the retrieval accuracy of MWR profiles [33]. Therefore, in this study, QC ERA5 RH profiles were utilized to fill temporal gaps in radiosonde data (outside of 08:00 and 20:00 LST), ensuring continuous data coverage for model training.

The final dataset comprised 8,667 quality-assured profiles, including data from MWR, MWCR, and ERA5, collected from 2018 to 2024. These profiles were randomly sampled by hour and split into training, validation, and testing sets in a 7:2:1 ratio. Specifically, the dataset consisted of 402 radiosonde profiles for training, 115 for validation, and 59 for testing.

Methodology

AngleNet

Following data preprocessing, the newly developed AngleNet for RH profile retrieval was trained using BT data captured across 14 channels at 8 distinct scanning angles (including one zenith angle and 7 oblique angles), as illustrated in Fig. 2. A dedicated "multi-angle-aware" module was designed to integrate the BTs from these scanning angles into a unified tabular format, allowing the model to process the data effectively. For linking MWR BTs with RH profiles, it is essential to transform the data into a structured tabular format. While traditional artificial intelligence (AI) models, such as RF, can process single-angle MWR channels in this format, they encounter noticeable challenges when data include channels from multiple scanning angles. Specifically, traditional AI models, such as LGBM and RF, are unable to recognize which data correspond to a particular angle. This presents a challenge, as each scanning angle captures the same atmospheric features, but from different perspectives. As a result, traditional models fail to fully exploit the multi-angle information, leading to a limited understanding of the MWR data and an inability to harness the full potential of observations from different angles.

Figure 2 illustrates the detailed architecture of AngleNet, which integrates MWR angle information with corresponding channel data and transforms these angle-dependent fused features, along with other global features, into embeddings for

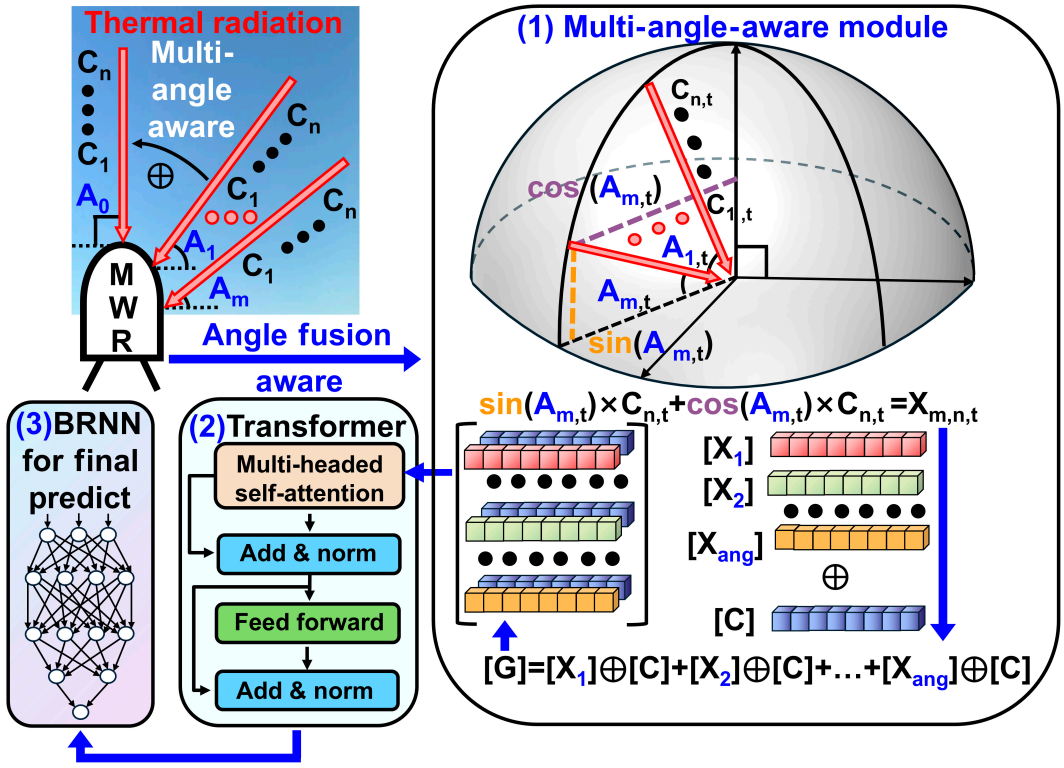

Fig. 2. Overall architecture of AngleNet.

transformer layers to capture complex dependencies. After data preprocessing, AngleNet can be divided into 3 key steps:

1. Multi-angle-aware module: This module combines the 14 channels of BT data with the corresponding angle information, enabling the model to effectively account for the angular dependencies in the data.
2. Transformer integration: The transformer technique is used to merge the angle-dependent fusion data with global features, allowing the model to capture long-range dependencies and interactions between the various input features.
3. RH profile retrieval: Finally, the integrated global features are passed into our previously proposed batch normalization and robust neural network (BRNN) [26] model, which is responsible for retrieving the RH profiles.

Specifically, for the multi-angle-aware module, we first designed sine- and cosine-based transform functions for MWR scanning angles to obtain the angle-aware variables (local feature):

$$X_{m,n,t} = sin(A_{m,t}) \times C_{n,t} + cos\left(A_{m,t}\right) \times C_{n,t} \quad (1)$$

where m is the elevation angle corresponding to the tth scanning from channel n of MWR, where $m \in [1, 2, \cdots, 8]$ and $n \in [1, 2, \cdots, 14]$. The final multi-angle-aware module for angle data is:

$$X_{ang}^{t} = \sum_{1}^{t} \left(X_{m,n} \times R_{m,n} + B_{m,n}\right), X_{ang}^{t} \in \mathbb{R}^{(m+n)\times d} \quad (2)$$

where X_{ang}^{t} is the tth continuous numerical input from channel n of MWR, $R_{n,t}$ is a real number vector $\mathbb{R}^{d}$, and $B_{n,t}$ is the feature bias.

In the multi-angle-aware module, a pointwise addition is conducted to superimpose the fused angle-aware data and conventional data:

$$X_{fus} = C \otimes X_{ang} = \left[\left(C_1^{1\times d} + X_{ang}^{1\times d}\right), \left(C_2^{1\times d} + X_{ang}^{1\times d}\right), \cdots \left(C_{m+n}^{1\times d} + X_{ang}^{1\times d}\right)\right] \in \mathbb{R}^{(m+n)\times d} \quad (3)$$

A real number matrix, called the global feature $G \in \mathbb{R}^{(m+n)\times d}$, is then appended to:

$$G_0 = Concat\left[G, X_{fus}\right] \quad (4)$$

G_0 is then processed by the transformer layers:

$$G_i = F_i\left(G_{i-1}\right) \quad (5)$$

The final representation of G^T is used by the BRNN model to retrieve RH profiles. The BRNN model consists of an input layer, 2 hidden layers [each includes a fully connected layer, a rectified linear unit (ReLU) layer, a batch normalization (BN) layer, and a dropout layer], and an output layer [26].

Feature selection and model training

BTs obtained from 14 channels at multiple angles, along with scanning elevation angle data that primarily describe the geometric relationships, are input into the "multi-angle-aware" module. This results in the generation of angle-aware variables (local features) that incorporate the correct angle information. Nevertheless, the optimal angles of BT data to be incorporated into the "multi-angle-aware" module remain unclear, and the relative contribution of each angle to the final retrieval process

is not yet fully understood. To resolve this ambiguity, we analyzed the contributions of both MWR channel features and angle features, utilizing feature importance parameters derived from the LGBM model.

As shown in Fig. 3A, the colored bar chart illustrates the feature importance of each frequency across elevation angles, with the bars arranged in descending order from 90° to 5°. The chart reveals that BTs at all elevation angles contribute to the retrieved RH profiles, with the highest importance observed at 90°, followed by 30° and 19.2°, which aligns with physical principles. SHapley Additive exPlanations (SHAP) analysis [48] corroborates these findings, with the largest SHAP values occurring at 30° and 19.2° among the oblique scanning angles, as shown in the inner subgraph of Fig. 3A and Fig. S1. The importance of angles below 14.4° decreases sharply, stabilizing below 10%.

Interestingly, the V-band channels demonstrate a stronger influence at higher angles (90° and 30°), whereas the K-band channels exhibit a more pronounced effect at lower angles (19.2° and below). To assess the collinearity of BTs across different angles, the variance inflation factor (VIF) was calculated for each channel across all angles. The angle-specific VIFs were subsequently averaged and ranked in ascending order, as shown in the gray section on the right side of Fig. 3B. The VIFs for the angles 90°, 30°, and 19.2° demonstrate a clear pattern of lower collinearity, highlighting the distinct roles that these angles play in the retrieval process. Therefore, in the angle feature selection process, priority should be given to angles with high feature importance and low VIF, such as 90°, 30°, and 19.2°. Lower angles, with less feature importance and higher collinearity, are excluded from the "multi-angle-aware" module to streamline AngleNet without losing critical information.

Additionally, we evaluated the performance of including BTs from multiple angles in the "multi-angle-aware" module, as summarized in Table S2. AngleNet achieved optimal performance when BTs from 90° in zenith pointing were combined with oblique elevation angles both 30° and 19.2°. Subsequently, angle-aware variables (local feature) and global feature were used as the independent variables. The global features included BTs from multiple MWR channels (a total of 14 × 8 channels) without angle information and surface meteorological data such as pressure, temperature, and RH. RH profiles from radiosonde and QC ERA5 were used as the dependent variables. Additionally, categorical variables such as location, month, and hour were included. All of these inputs were fed into the transformer and BRNN, as detailed in Table S3.

Optimization of hyperparameters in AngleNet

As demonstrated in many previous studies [26,49,50], the 5-fold CV method is widely used in machine learning for optimizing hyperparameters and validating model generalization performance [51]. The outcome of the CV process that yields the optimal performance is selected as the final result, and detailed results from each CV round are summarized in Table S4. The validation dataset plays an essential role in fine-tuning the hyperparameters of AngleNet. The final hyperparameter values for AngleNet are presented in Table S5. To prevent overfitting, we have employed several measures including dropout layers and early stopping guided by training and validation loss curves, with the training loss function shown in Fig. S2. The dropout method has been demonstrated to obviously reduce overfitting and improve the performance of neural networks [26]. Following the training phase, the model is utilized to generate hourly RH profiles across 3 cities (Beijing, Nanjing, and Shanghai) from 2018 to 2024. These generated profiles are subsequently compared with the radiosonde RH profiles in the test dataset excluded from the model training process to verify the

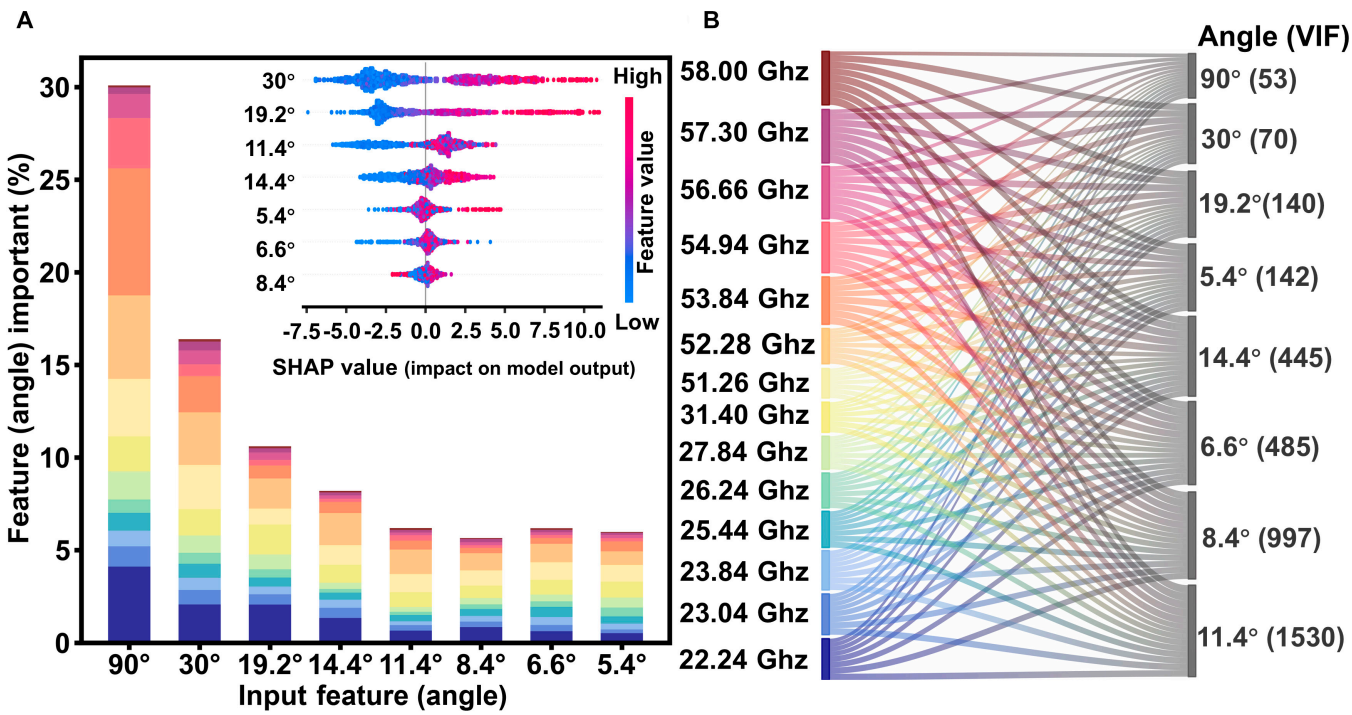

Fig. 3. Input (A) feature (angle) importance from LGBM (subgraph presents the SHAP values of each feature) and (B) angle VIF. The color from top to bottom (purple to dark blue) represents the feature importance (A) or the logarithm of VIF (B) of the 14 channels for each elevation angle, organized in descending order by frequency from highest (V-band oxygen channels) to lowest (K-band water vapor channels).

generalization ability of AngleNet. The definitions of the evaluation metrics are provided in Text S3.

Comparison

In this study, we compared the performance of our proposed AngleNet in comparison to conventional machine learning models, such as LGBM and RF, as well as the original MWR products. LGBM, recognized for its scalability and efficiency in handling high-dimensional data [52,53], and RF, recognized for its ability to model complex interactions and maintain robustness in high-dimensional datasets[26,54], provided a solid baseline for evaluating AngleNet's performance. Traditional MWR retrieval methods are typically based on neural networks or linear regression [55]. Furthermore, the manufacturer has not provided accuracy details for RH profile retrieval, as RH is derived from a combination of absolute humidity profiles obtained via zenith pointing mode and temperature profiles generated from both zenith pointing and elevation scanning mode measurements [2]. These various models differ in terms of network structure, complexity, and prediction mechanisms, which ensure the robustness and generality of the results presented in this study.

Results

Comparison with four retrieval methods

To comprehensively assess the performance of the proposed AngleNet model proposed in this study, Fig. 4 and Table 1 present the overall accuracy of RH predictions obtained by AngleNet compared with other methods, based on the 5-fold CV validation dataset, which comprises conventional radiosonde observations collected at 2 daily intervals (08:00 and 20:00 LST) across 3 cities (Beijing, Nanjing, and Shanghai) from 2018 to 2024. Figure 4A to C presents the RH values retrieved by AngleNet, LGBM, and RF using multi-angle BTs, compared to radiosonde measurements across 115 atmospheric vertical layers up to 10 km. The high kernel density values, highlighted in red, indicate regions where most of the data are concentrated. As shown in Fig. 4A, the linear regression between the RH retrieved by AngleNet and the radiosonde RH yields a slope of 0.77, a y intercept of 7.16, an R^2 of 0.71, and a root mean square error (RMSE) of 10.39. Notably, over 74.84% of the data fall within the ±10% error envelope (EE). This marks a 30.73% reduction in RMSE compared to the maximum allowable RMSE of 15% specified by the current MWR industry standard (QX/T 504-2019) in China.

In comparison to traditional machine learning models, such as LGBM and RF, AngleNet demonstrates substantial improvements: R^2 increases by 11% over LGBM and 26% over RF, while RMSE decreases by 11% and 19%, respectively. This leads to a higher proportion of the data falling within the EE, with improvements of 23% relative to LGBM and 26% relative to RF. Notably, these gains are particularly pronounced in the retrieval of high RH values (above 60%). In contrast, Fig. 4D and F shows the RH values retrieved by LGBM, RF, and original MWR products using only zenith-angle BTs, compared to radiosonde measurements. When comparing these results to Fig. 4A and C, the introduction of multi-angle BTs does not yield obvious improvements for LGBM and RF models. However, the integration of multi-angle data clearly enhances the performance of AngleNet, particularly in the retrieval of high RH values.

Finally, RF, using only zenith angle BTs, is selected as the baseline model to compare the improvement of various models across 3 cities, further demonstrating the advancements achieved by AngleNet, as shown in Fig. 4G. The colors, ranging from dark to light, represent the results from AngleNet, LGBM, and RF using multi-angle BTs, as well as LGBM using only zenith-angle BTs. The red bars outside the circle indicate the relative improvement in R^2, while the blue bars inside the circle represent the relative reduction in RMSE, both compared to the baseline model. The comparison with the baseline model results indicates that AngleNet achieves substantial improvements in both accuracy and robustness. Specifically, R^2 shows a relative improvement of 24% to 40%, while RMSE is relatively reduced by 19% to 36% at 3 cities. Despite the influence of spatial difference, the performance improvement shows only slight variation. However, AngleNet consistently yields the best results across all cities, as also demonstrated in Table 1.

Table 1 provides the specific statistical results of the retrieved RH profiles from various methods, compared to radiosonde measurements for evaluating overall performance. The table also presents the results for each city. Notably, the RH retrieval results from AngleNet in Beijing are compared with those obtained using our previous BRNN method [26], which only utilizes zenith-angle BTs. The results show a 41% relative improvement in R^2 and a 10% reduction in RMSE. These findings underscore the effectiveness of AngleNet in integrating multi-angle information from MWR, enabling it to capture the complex nonlinear relationships between BT and RH across diverse locations.

Independent validation

To illustrate and compare the outcomes of different retrieval methods, 6 cases from 3 cities were selected. Radiosonde measurements serve as the reference for evaluating the performance of the retrieval methods. Figure 5 present comparisons of the retrieved RH profiles with radiosonde data at 08:00 and 20:00 LST, respectively, in the same sample-based 5-fold CV validation dataset. The retrieved RH profiles generally align with the radiosonde data in terms of altitude variation, but only AngleNet accurately captures the overall trend of the radiosonde RH profiles.

To further assess the efficacy of AngleNet in retrieving RH profiles beyond the regular radiosonde observation times, an additional independent validation was conducted using 27 encrypted radiosonde measurements from Nanjing and Shanghai, collected outside the usual 08:00 and 20:00 LST periods, and the results as shown in Fig. 6 and Table 2. Notably, the additional radiosonde measurements were conducted at times outside the regular measurement periods, and the corresponding ERA5 RH profiles for these additional periods were excluded from the modeling process. This approach ensures a thorough evaluation of AngleNet's ability to generalize to unobserved times.

The precise locations and dates for the encrypted radiosonde measurements are detailed in Fig. 6A, along with schematic diagrams illustrating the release process of the radiosonde balloons during both daytime and nighttime. Additionally, as shown in Fig. 6B and C, AngleNet achieved R^2 values of 0.57 in Nanjing and 0.63 in Shanghai, with RMSE values of 11.26 and 12.91, respectively. In both cities, 60.24% of the data in Nanjing and 73.10% in Shanghai fell within the ±10% EE. The scatterplots highlight the concentration of data points, with high-density regions marked in red, and the kernel density estimates (KDEs) on the sides of the scatterplots further illustrate the distribution of the data in both cities. The shape of the RH distribution inverted by AngleNet is roughly consistent with that measured by radiosonde, with most data

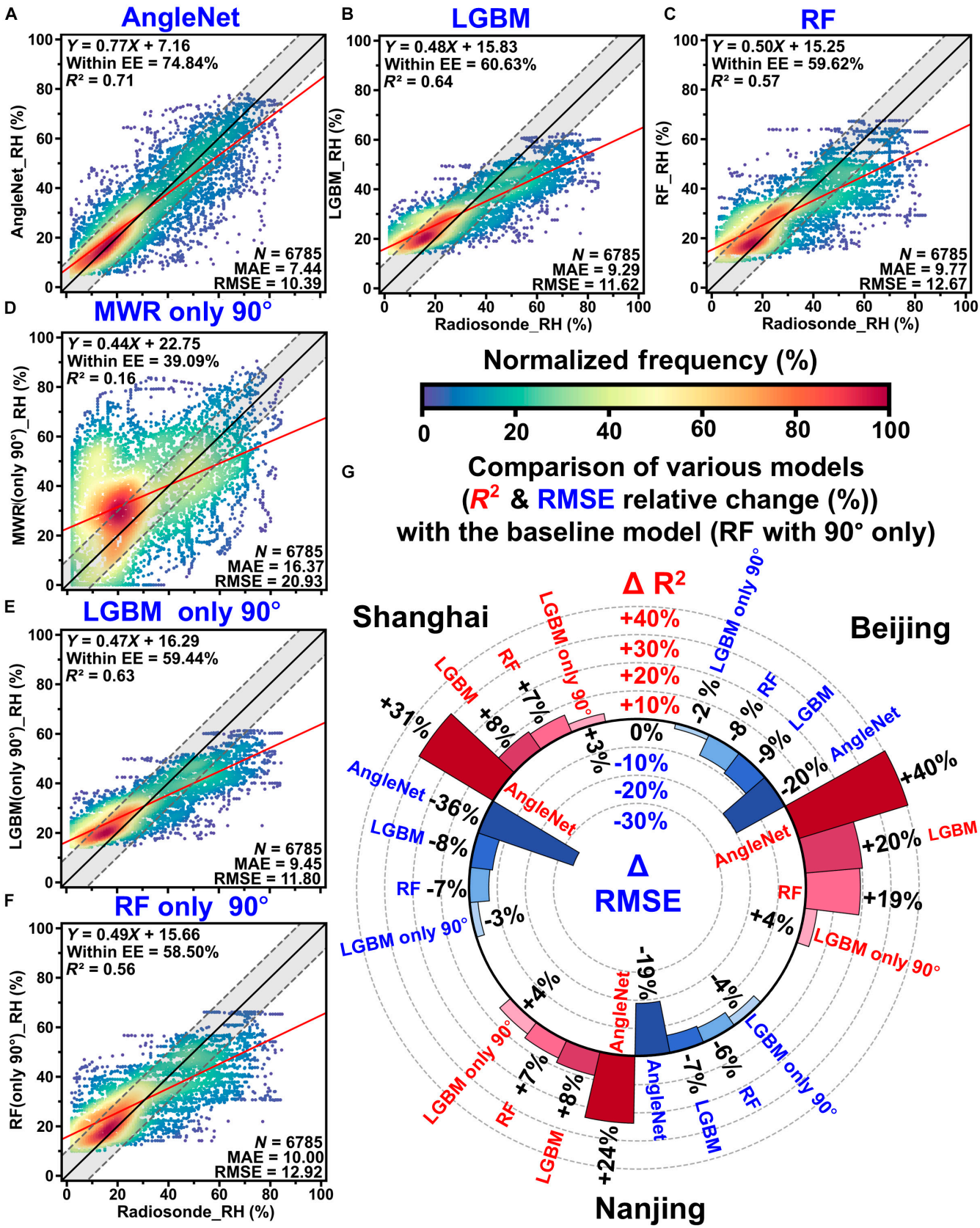

Fig. 4. Density scatterplots of RH from radiosondes and the (A) AngleNet, (B) LGBM, (C) RF, (D) original MWR products with input data only in 90°, (E) LGBM with input data only in 90°, and (F) RF with input data only in 90°. The black dashed line represents the 1:1 relationship, the red solid line represents the best linear fitting line, and 2 gray dotted lines delineate the expected error (EE) envelope of ± (10%). R^2 is the coefficient of determination, N is the total number of data points, MAE is the mean absolute error, and RMSE is the root mean square error. (G) Comparison of R^2 (red) and RMSE (blue) from various models with the baseline model (RF with input data only in 90°) across cities. The numbers represent the relative difference between various models with the baseline model.

Table 1. Comparison of the RH performance with radiosonde of 4 methods in 3 sites

Sites	Model	R^2	RMSE	MAE	Within EE [± (10%)]
All	AngleNet	**0.71**	**10.39**	**7.44**	**74.84%**
	LGBM	0.64	11.62	9.29	60.63%
	LGBM (only 90°)	0.63	11.80	9.45	59.44%
	RF	0.57	12.67	9.77	59.62%
	RF (only 90°)	0.56	12.92	10.00	58.50%
	Original MWR products (only 90°)	0.16	20.93	16.37	39.09%
Beijing	AngleNet	**0.62**	**10.53**	**7.50**	**72.76%**
	LGBM	0.58	11.04	8.51	66.65%
	LGBM (only 90°)	0.57	11.21	8.64	64.94%
	RF	0.48	12.31	9.22	62.48%
	RF (only 90°)	0.47	12.40	9.36	60.71%
	Original MWR products (only 90°)	0.21	20.94	16.29	39.88%
Nanjing	AngleNet	**0.74**	**10.82**	**7.82**	**73.08%**
	LGBM	0.66	12.30	10.06	55.20%
	LGBM (only 90°)	0.65	12.58	10.25	54.87%
	RF	0.61	13.19	10.21	58.59%
	RF (only 90°)	0.59	13.57	10.51	58.51%
	Original MWR products (only 90°)	0.17	19.31	15.07	41.41%
Shanghai	AngleNet	**0.83**	**8.97**	**6.47**	**84.35%**
	LGBM	0.71	11.70	9.82	55.22%
	LGBM (only 90°)	0.70	11.74	10.03	53.65%
	RF	0.66	12.59	10.36	53.74%
	RF (only 90°)	0.64	12.93	10.71	52.26%
	Original MWR products (only 90°)	0.23	23.95	19.36	32.00%

R^2, coefficients of determination; RMSE, root mean square error; MAE, mean absolute error

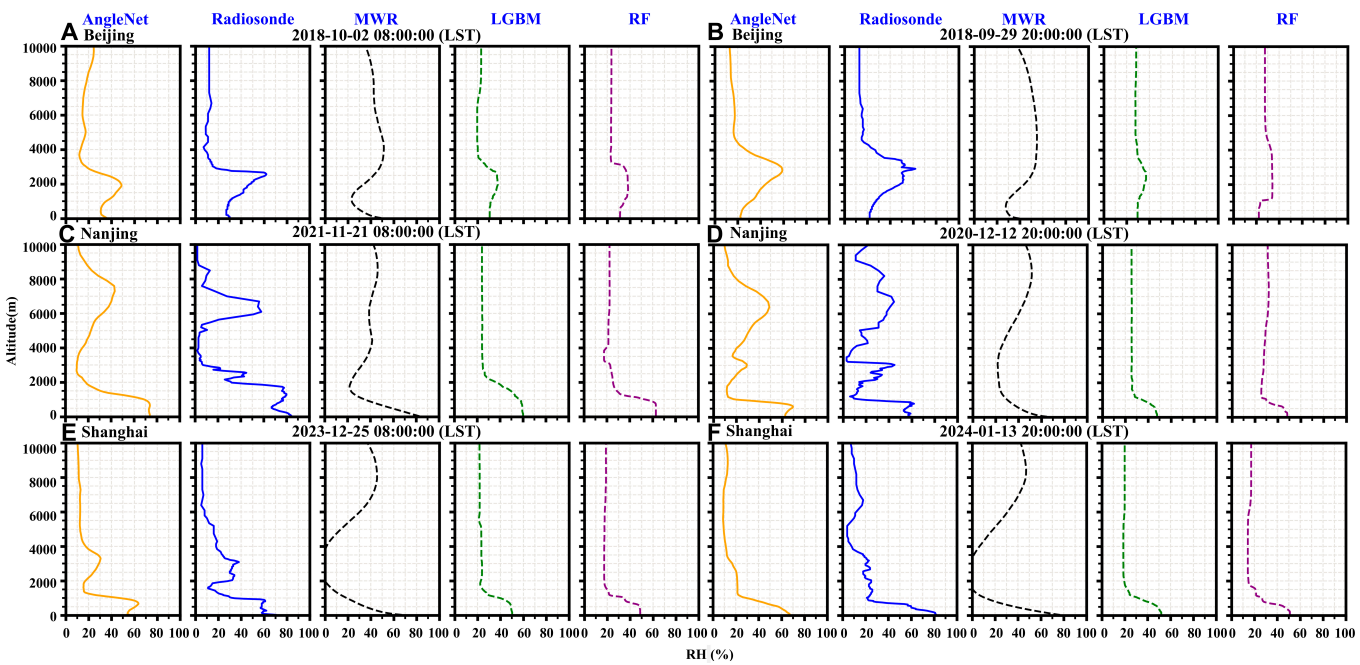

Fig. 5. Comparison of RH profiles generated by AngleNet, radiosonde, MWR, LGBM, and RF methods at 08:00 LST and 20:00 LST under clear-sky conditions for (A and B) Beijing, (C and D) Nanjing, and (E and F) Shanghai.

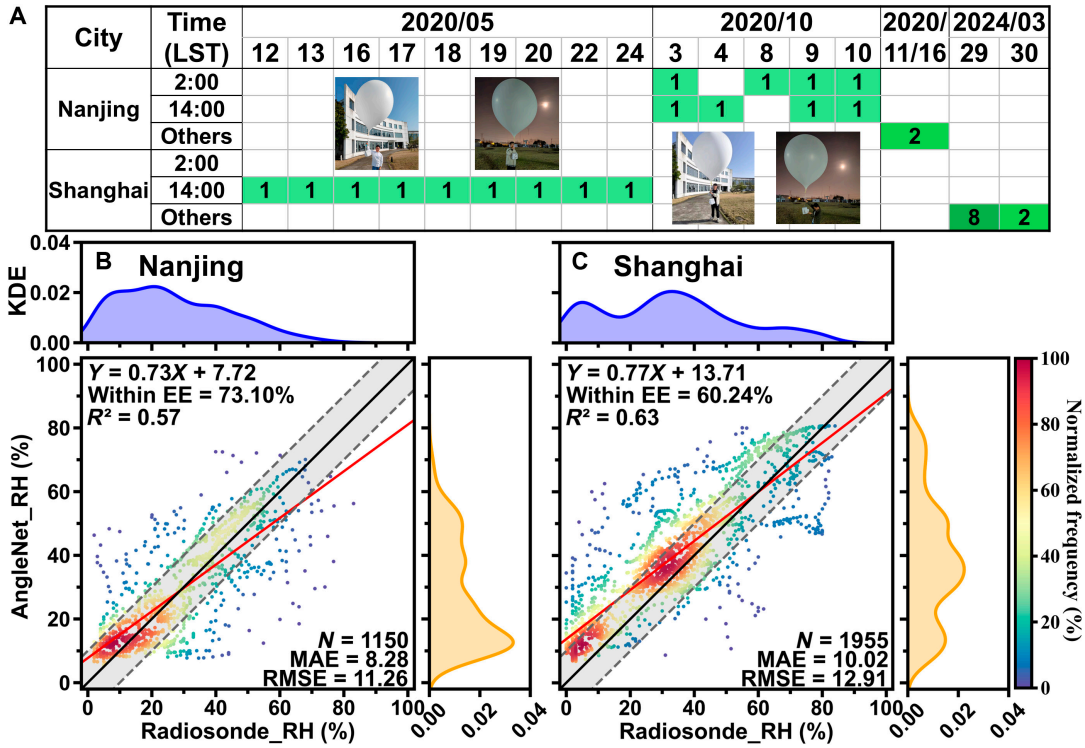

Fig. 6. Additional independent verification of RH profiles retrieved by AngleNet compared with radiosonde measurements. (A) Specific locations and dates where the color and number indicate the frequency of radiosonde balloon releases, with darker colors representing a higher frequency of releases. Radiosonde balloon releases during daytime or nighttime are illustrated in the blanks of (A), while (B) Nanjing and (C) Shanghai present density scatterplots of additional independent verification. The black dashed line represents the 1:1 relationship, the red solid line represents the best linear fitting line, and 2 gray dotted lines delineate the expected error (EE) envelope of ± (10%). The blue and orange lines represent KDE RH profiles from radiosondes and AngleNet, respectively.

concentrated in the 20% to 80% RH range. Table 2 further details the comparative performance of AngleNet and alternative methods using encrypted radiosonde data. Interestingly, for these validation metrics of RH profiles, AngleNet indicated superior performance in sample-based 5-fold CV compared to independent validation. This discrepancy may be caused by training datasets employed during temporal gaps in radiosonde observations, which were derived from QC ERA5 RH profiles. Such datasets, while valuable, exhibit slightly lower representativeness compared to real-time radiosonde observations. Nonetheless, as evidenced in Table 2, AngleNet consistently better than LGBM, RF (using multiple angles), and the original MWR products (90° only) in independent validations over Nanjing and Shanghai, with higher R^2, more data within the ±10% EE, and lower RMSE and MAE. Overall, AngleNet can obtain relatively high-accuracy RH profiles in all periods, further validating its generalization performance.

Bias, RMSEs, and MAE variation with altitude

The RH profile retrieval bias, RMSE, and MAE (mean absolute error) from various techniques are presented in Fig. 7, based on the same 5-fold CV validation dataset as utilized in Fig. 4 and Table 1. Figure 7A shows that the bias of AngleNet remains within ±10% from the surface up to 10 km. The mean bias for AngleNet is generally close to the median at lower altitudes. Additionally, below 2.5 km, the maximum RH bias increases with altitude but remains relatively stable above 2.5 km. In comparison to the other models, which are demonstrated in Fig. 7B to F, AngleNet exhibits the smallest box length across all 4 methods from the surface to 10 km, and its mean bias is consistently closer to the median than those of the other models. Furthermore, we compare the RMSEs and MAEs of the RH retrievals from the 4 methods at different altitudes, as shown in Fig. 7G and H. This comparison highlights the differences in RH retrieval performance across various altitude layers. For all 4 methods, both RMSE and MAE generally increase with altitude from the surface to 10 km, with the maximum deviations occurring above approximately 2.5 to 3.5 km. Notably, AngleNet exhibits the smallest RMSE and MAE across the entire altitude range, particularly at lower altitudes, while the higher RMSE and MAE values observed at middle and upper altitudes align with those reported in previous studies [21,34,56]. Overall, these results indicate that AngleNet provides superior RH retrieval performance compared to the other methods.

Moisture transport insights from AngleNet

Figure 8 presents an independent validation case conducted in Nanjing, covering the period from 16:00 on 2020 November 8 to 23:00 on 2020 November 10 (LST), incorporating MWR observations at a 5-min interval and including 4 times encrypted radiosonde measurements. This case illustrates the process of moisture transport, including the evolution of a high-RH air mass as it moves across the region and eventually dissipates, as well as the lifting of high-RH stratification at low altitudes, likely influenced by diurnal variations in the planetary boundary layer (PBL). The radiosonde data (Fig. 8A) reveal dynamic, true RH profiles over time, providing a baseline for evaluating the performance of

Table 2. Comparison of the RH performance with radiosonde of 4 methods in encrypted radiosonde measurements

Sites	Model	R^2	RMSE	MAE	Within EE [± (10%)]
Nanjing	AngleNet	**0.57**	**11.26**	**8.28**	**73.10%**
	LGBM	0.48	13.48	10.46	51.26%
	RF	0.44	14.34	11.33	50.17%
	Original MWR products (only 90°)	0.15	22.37	17.16	40.34%
Shanghai	AngleNet	**0.63**	**12.91**	**10.02**	**60.24%**
	LGBM	0.51	13.17	12.09	35.15%
	RF	0.46	13.32	12.96	31.83%
	Original MWR products (only 90°)	0.19	25.15	23.07	22.66%

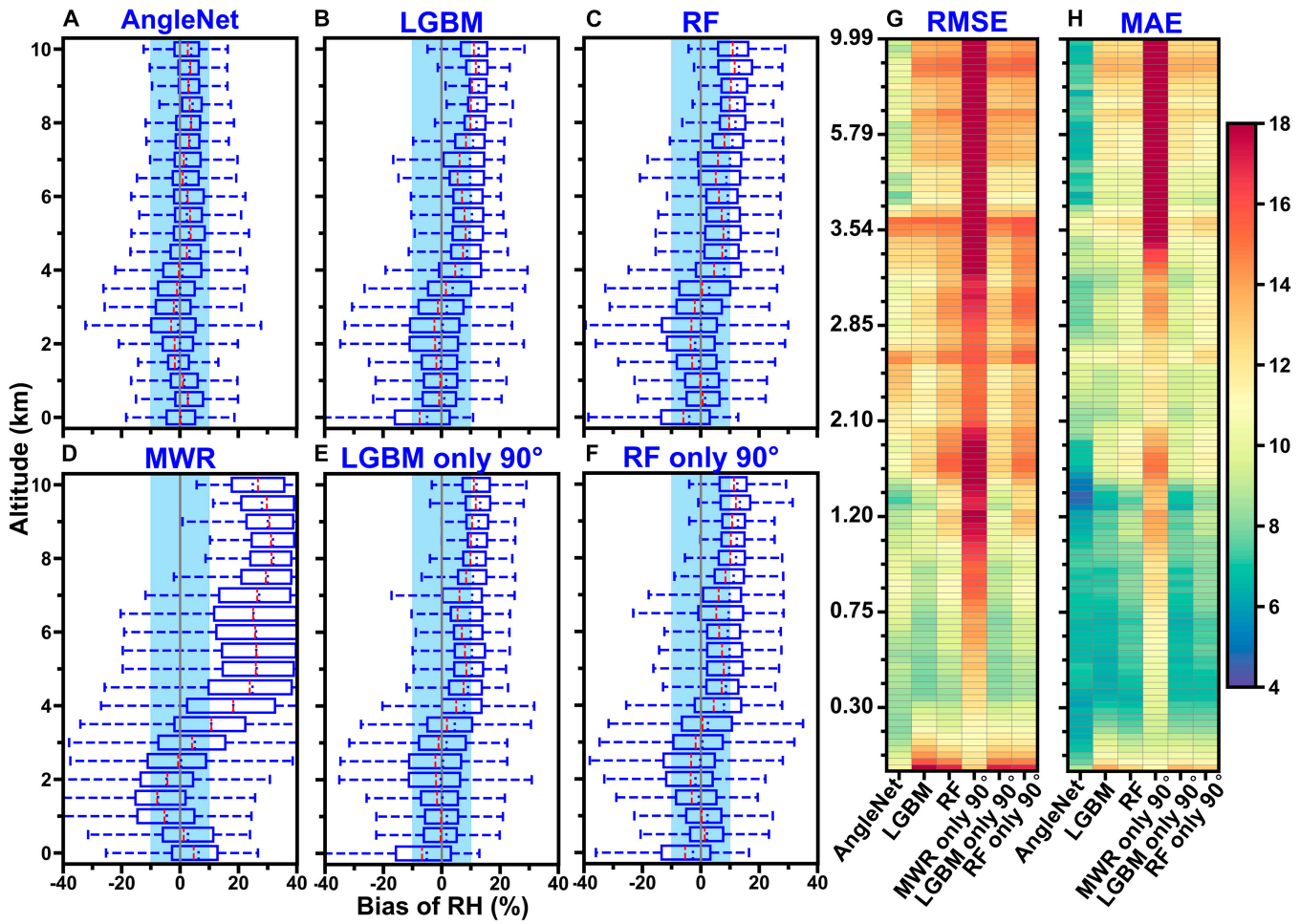

Fig. 7. RH retrieval bias (retrieval from models minus radiosonde) by the (A) AngleNet, (B) LGBM, (C) RF, (D) original MWR products with input data only in 90°, (E) LGBM with input data only in 90°, and (F) RF with input data only in 90°. Figure 7 is based on the same sample-based 5-fold CV validation dataset as utilized in Fig. 4 and Table 1. The means, medians, and 75% (1−σ) intervals are shown as red dotted lines, blue lines within the boxes, and the boxes themselves, respectively. The blue shadow means ±10% bias of RH. The gray lines are 0 error lines (500-m vertical intervals). (G) and (H) are the profile retrieval RMSEs and MAEs for RH with radiosonde dates (original vertical intervals), respectively.

AngleNet. AngleNet (Fig. 8B) effectively captures both temporal and vertical variations, demonstrating strong consistency with the radiosonde measurements. In contrast, traditional MWR retrievals (Fig. 8C) reflect only broader trends and fail to resolve finer structural details, while the validation metrics (Fig. 8D) demonstrate the robustness of AngleNet, with an R^2 of 0.77 between AngleNet and the radiosonde data, 84.35% of the data falling within the ±10% EE, and an RMSE of 9.24. The

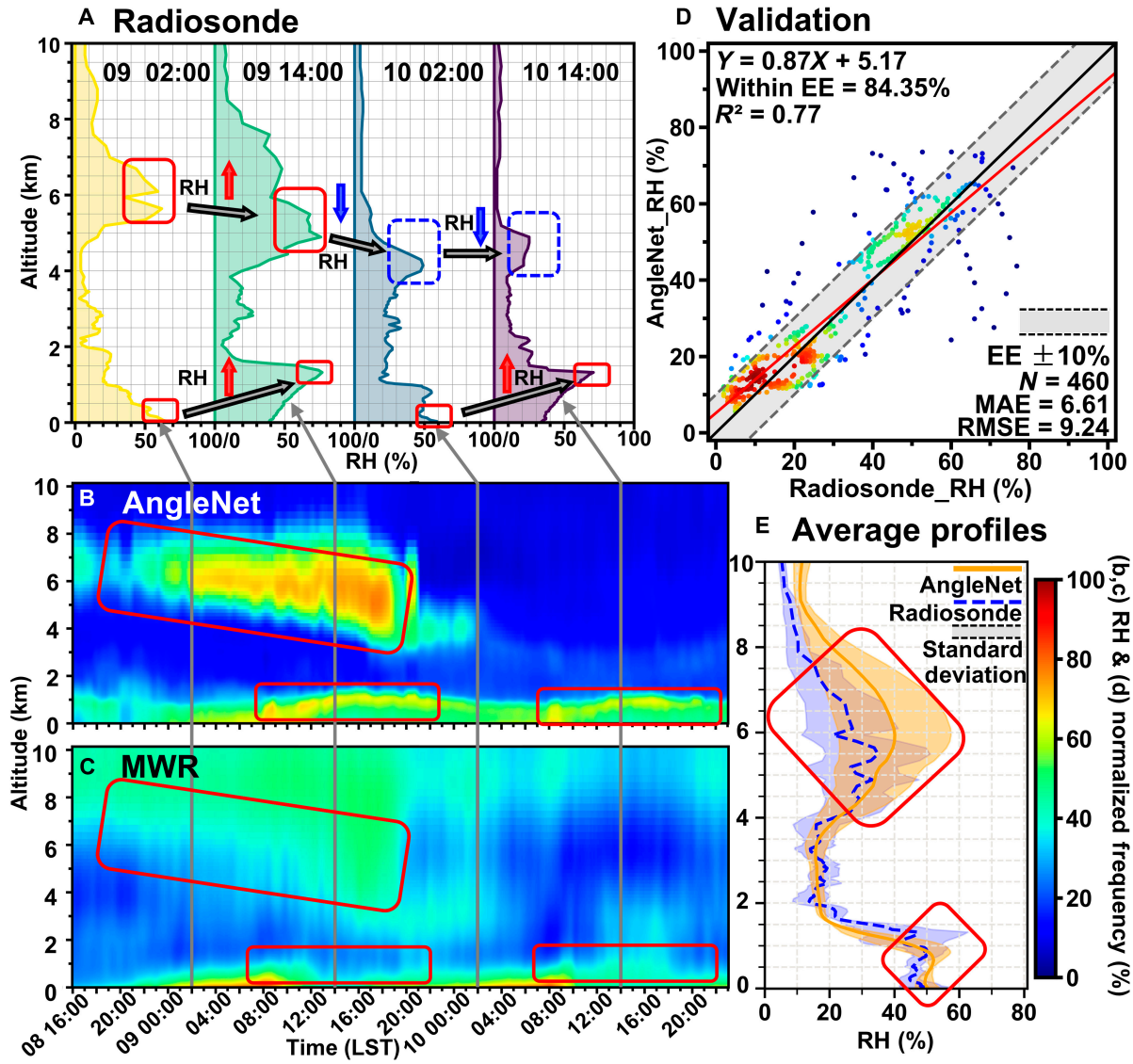

Fig. 8. Additional independent validation case in Nanjing from 16:00 on 2020 November 08 to 23:00 on 2020 November 10 (LST) to verify the applicability of retrieved RH profiles. (A) Radiosonde measurements taken at 02:00 and 14:00 (LST). (B) AngleNet RH profile time series with a 5-min interval across 115 vertical layers, where gray arrows represent the corresponding time of radiosonde. (C) Original MWR RH profile products at the same 5-min interval and vertical layering. (D) Validation results comparing 4 times RH profiles from AngleNet and radiosonde. The black dashed line represents the 1:1 relationship, the red solid line represents the best linear fitting line, and 2 gray dotted lines delineate the expected error (EE) envelope of ± (10%). (E) Average RH profiles of AngleNet and radiosonde at 4 times. The orange solid and blue dotted line represents the mean RH profiles from AngleNet and radiosonde, while the corresponding shaded interval represents the standard deviation (SD).

averaged RH profiles (Fig. 8E) further highlight the consistency of AngleNet with the radiosonde data, particularly in capturing key atmospheric vertical features, such as the high-RH layer around 6 km and the accumulation layer near the top of the PBL. A detailed comparison of individual radiosonde measurements and AngleNet retrievals is provided in Fig. S3 and Table S6.

AngleNet for revealing dry wet stratification uplift

Figure 9 presents another independent validation case in Shanghai, covering the period from 08:00 on 2024 March 29 to 05:00 on 2024 March 30 (LST), incorporating MWR observations at a 5-min interval and including 8 times encrypted radiosonde measurements within a 24-h period. To provide high-resolution baseline radiosonde data, 8 radiosonde balloons were deployed within a single day. This case illustrates the continuous evolution of dry stratification uplift at low altitudes, likely driven by diurnal variations in the PBL. The radiosonde observations (Fig. 9A) reveal detailed vertical RH structures over time, offering a clear depiction of the uplift process. AngleNet (Fig. 9B) effectively captures both temporal and vertical variations, demonstrating strong consistency with the radiosonde data. In contrast, traditional MWR retrievals (Fig. 9C) fail to accurately reflect these trends, missing critical details, especially at low altitudes. The validation metrics (Fig. 9D) further confirm the robustness of AngleNet, with an R^2 of 0.62, 72.14% of the data falling within the ±10% EE, and an RMSE of 9.65. The averaged RH profiles (Fig. 9E) highlight the consistency of AngleNet with radiosonde data, particularly in characterizing the uplift of 2 distinct dry layers near the top of the PBL at low altitudes. A detailed comparison of individual radiosonde measurements and AngleNet retrievals is provided in Fig. S4 and Table S7.

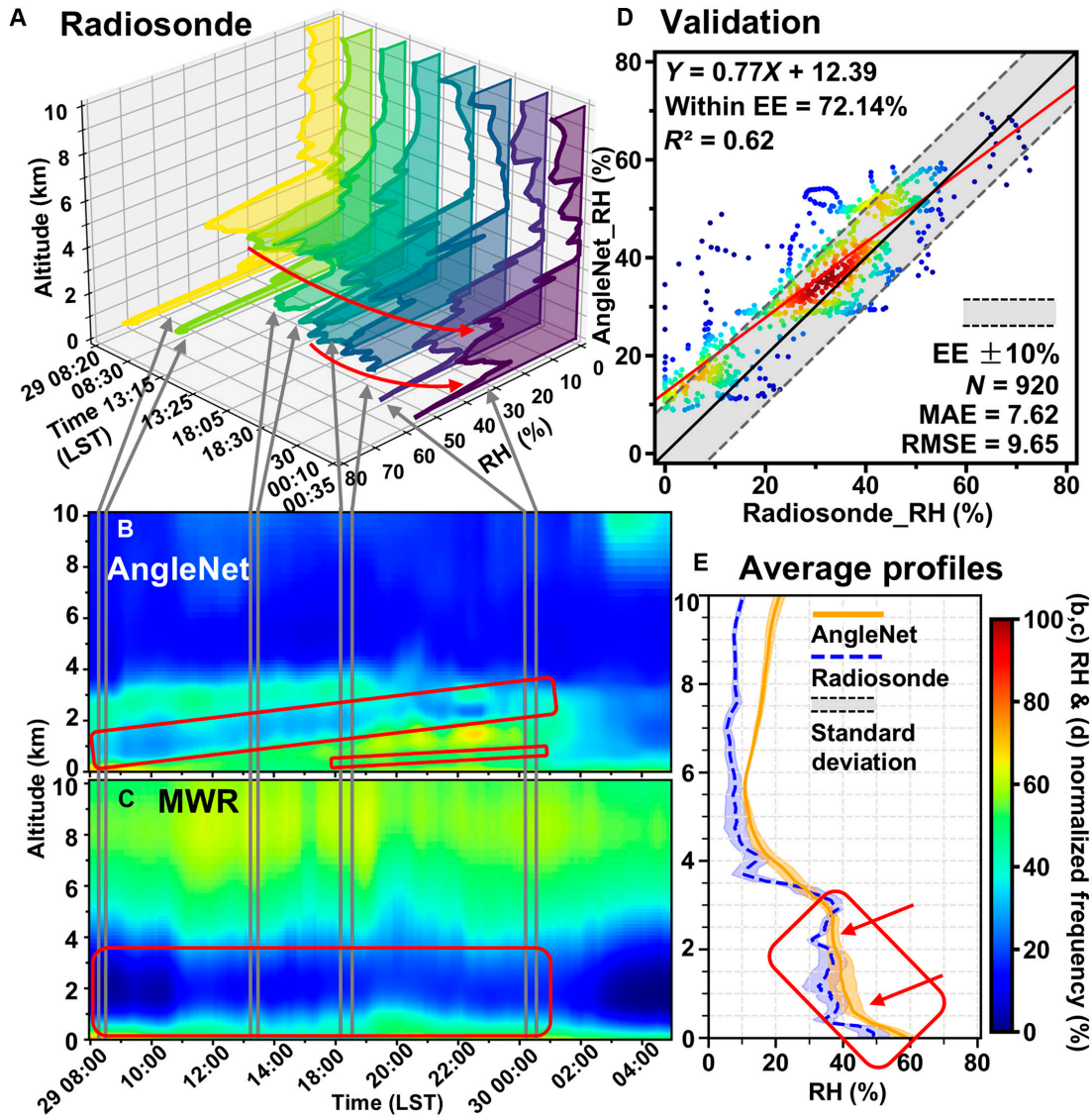

Fig. 9. Additional independent validation case in Shanghai from 08:00 on 2024 March 29 to 05:00 on 2024 March 30 (LST) to verify the applicability of retrieved RH profiles. (A) Radiosonde measurements taken 8 times within 24-h period. (B) AngleNet RH profile time series with a 5-min interval across 115 vertical layers, where gray arrows represent the corresponding time of radiosonde. (C) Original MWR RH profile products at the same 5-min interval and vertical layering. (D) Validation results comparing 4 times RH profiles from AngleNet and radiosonde. The black dashed line represents the 1:1 relationship, the red solid line represents the best linear fitting line, and 2 gray dotted lines delineate the expected error (EE) envelope of ± (10%). (E) Average RH profiles of AngleNet and radiosonde at 4 times. The orange solid and blue dotted line represents the mean RH profiles from AngleNet and radiosonde, while the corresponding shaded interval represents the SD.

Discussion

Our findings are important for several important reasons, each representing a crucial step forward in atmospheric profile retrieval. Firstly, AngleNet overcomes the inherent limitations of conventional machine learning models by innovating its novel multi-angle-aware architecture. By accurately matching angle information with BT data, AngleNet effectively capitalizes on multi-angle data that were previously underexploited. This is in stark contrast to conventional models that rely solely on vertically oriented BT data [21,26,28,33,34,57], overlooking oblique scanning angles, limiting their ability to capture atmospheric variations, particularly near the surface, where temperature and moisture gradients are most dynamic. By integrating multi-angle data, AngleNet enhances its sensitivity to these variations, thereby substantially improving the accuracy of retrieving RH profiles while preserving temporal continuity.

This improvement in retrieval accuracy is especially critical in the lower atmosphere, where fine-scale structures such as PBL and moisture gradients play pivotal roles in atmospheric thermodynamics. Traditional models fail to resolve these structures adequately, primarily because they cannot leverage the complex nonlinear relationships between BT and RH profiles at lower altitudes. AngleNet, in contrast, addresses this challenge by integrating multi-angle observations that capture these nonlinear dependencies more effectively. This ability to incorporate multiple perspectives—literally and figuratively—represents a substantial step forward in atmospheric remote sensing and highlights the value of exploiting underutilized data sources.

Second, AngleNet capitalizes on the fundamental properties of ground-based radiometry and the physical principles

underlying multi-angle observations [10]. The differential absorption of multi-frequency and multi-angle observations is essential for comprehending the vertical distribution of atmospheric thermodynamics. By integrating data from oblique scanning angles, where longer optical paths amplify absorption and emission effects [30], AngleNet enhances its sensitivity to near-surface atmospheric conditions, which is crucial for detecting subtle atmospheric features that traditional vertical-only measurements cannot capture, such as the dry and wet stratification of the atmosphere and low-altitude atmospheric stability.

Thirdly, retrieval uncertainties under cloudy conditions arise from physical constraints associated with passive remote sensing. MWR derives RH profiles by measuring atmospheric BT. However, in cloud-covered scenarios, clouds exhibit semi-transparent characteristics at microwave frequencies due to scattering and absorption processes, introducing non-negligible perturbations to BT measurements and thus markedly increasing retrieval uncertainty [3,58]. While synergistic use of MWR and infrared radiometers can be used to estimate the liquid water path with reasonable accuracy, this approach lacks the vertical resolution to resolve cloud optical properties at different altitudes. Consequently, clouds with varying vertical extents may yield similar BT signatures when observed by MWRs. This inherent physical limitation introduces prodigious uncertainty into RH profile retrieval under cloudy scenarios. To mitigate these limitations, future research should consider integrating additional observational instruments, such as cloud radar or lidar, which can deliver detailed cloud-profile information. Such integration would obviously enhance the accuracy of RH retrievals under cloudy conditions, particularly in pre-convective environments [59].

Finally, compared to physical retrieval methods that also utilize multi-angle BT data [3,11,22,30], AngleNet not only attains comparable accuracy levels but also provides marked merits in computational efficiency. On average, AngleNet retrieves RH profiles (with 115 vertical layers) in less than 100 ms per profile using a graphics processing unit (NVIDIA RTX 4090). In contrast, traditional physical methods rely on solving the radiation transfer equation to forward model RH profiles. As the radiative transfer equation is inherently an integro-differential equation, it lacks an exact analytical solution in realistic atmospheric conditions [58]. Consequently, traditional physical methods often demand extensive computational resources and complex numerical modeling to process data, which restrict their applicability. In contrast, AngleNet minimizes computational complexity through its optimized architecture, enabling faster processing times without compromising accuracy. This is an advantage, particularly in operational settings where timely data retrieval is essential for atmospheric monitoring and forecasting. Moreover, AngleNet excels in capturing nonlinear dependencies between BT and RH profiles, a critical feature for accurate atmospheric profile retrieval in the presence of complex environmental conditions.

AngleNet substantially improves RH profile retrieval accuracy, further reinforcing the role of MWR as a powerful tool for atmospheric observation and research. This further solidifies the use of MWR as a powerful and reliable tool for atmospheric observation and scientific inquiry. The improved retrieval accuracy achieved by AngleNet can help provide deeper insights into atmospheric thermodynamics, enabling better characterization of atmospheric moisture transport, PBL, and cloud processes. These improvements are pivotal for advancing our understanding of key atmospheric phenomena, such as precipitation forecasting, weather patterns, and the impacts of climate change. AngleNet is expected to substantially enhance both the scientific and practical value of the existing global meteorological observation network.

Conclusion

This study introduces an innovative deep learning model, called AngleNet, to substantially enhance the retrieval accuracy of RH profiles from ground-based MWRs. The experimental findings demonstrate the superiority of AngleNet over traditional approaches, achieving an average R^2 of 0.71 and an RMSE of 10.39 across 3 validation sites in China. AngleNet consistently outperforms conventional machine learning models, such as LGBM ($R^2 = 0.64$) and RF ($R^2 = 0.57$), with an average increase in R^2 exceeding 10% and reductions in RMSE and MAE by more than 10%. These findings underscore AngleNet's robustness and superior ability to capture intricate atmospheric variations, outperforming existing methods. Specifically, in Beijing, a direct comparison with our previous BRNN method [26], which relied solely on zenith-angle BTs, reveals that AngleNet achieves a 41% relative improvement. Notably, AngleNet demonstrates a 30.73% reduction in RMSE compared to the maximum allowable RMSE of 15% specified in the current MWR industry standard (QX/T 504-2019) in China, marking a remarkable step forward in operational atmospheric profiling. Furthermore, supplementary independent validation using 27 encrypted radiosonde observations collected outside regular observation periods in Nanjing and Shanghai revealed favorable correlations, further emphasizing the robust applicability of AngleNet across the entire day.

By leveraging BTs from multiple scanning angles, AngleNet overcomes the constraints of traditional models, like LGBM and RF, which are limited by their reliance on vertical observations, lack of angular awareness, and treatment of input features as independent. This markedly improved performance is primarily attributed to AngleNet's integration of multi-angle BT data and corresponding angular information through advanced "multi-angle-aware" module. Comprehensive feature analysis, including feature importance, SHAP values, and VIF, along with evaluations utilizing the "multi-angle-aware" module, reveals that the optimal RH retrieval performance is achieved by combining zenith angle BTs with oblique elevation angles of 30° and 19.2°. This multi-angle awareness allows AngleNet to effectively and consistently capture complex RH profile characteristics and improve its sensitivity to near-surface atmospheric conditions, representing a substantial breakthrough in ground-based remote sensing.

Acknowledgments

We would like to thank the Chinese Meteorological Administration's National Meteorological Information Center (http://data.cma.cn/) and Global Modeling and Assimilation Office (https://earthdata.nasa.gov) for the various datasets employed in this study. We also extend our gratitude to all those involved in the field observation activities for their unwavering dedication and collaboration.

Funding: This research was supported by the National Nature Science Foundation of China (42030606).

Author contributions: Y.Y. and X.Y. designed the research. Y.Y. collected and analyzed the data. Z.L. supervised the project. X.Y. acquired funding. Y.Y. and X.Y. wrote the manuscript with support from Z.L., J.G., Yuying Wang, H.W., Y.S., Ye Wang, and

L.Z. All authors discussed the results and contributed to the interpretation of the final manuscript.
Competing interests: The authors declare that they have no competing interests.

Data Availability

The codes of AngleNet and AngleNet RH profiles from 2018 to 2024 are available online at https://zenodo.org/records/14786838.

Supplementary Materials

Text S1 to S3
Fig. S1 to S4
Tables S1 to S7

References

1. Kotthaus S, Bravo-Aranda JA, Coen MC, Guerrero-Rascado JL, Costa MJ, Cimini D, O'Connor EJ, Hervo M, Alados-Arboledas L, Jiménez-Portaz M, et al. Atmospheric boundary layer height from ground-based remote sensing: A review of capabilities and limitations. *Atmos Meas Tech*. 2023;16(2):433–479.
2. Löhnert U, Turner DD, Crewell S. Ground-based temperature and humidity profiling using spectral infrared and microwave observations. Part I: Simulated retrieval performance in clear-sky conditions. *J Appl Meteorol Clim*. 2009;48(5):1017–1032.
3. Bianco L, Adler B, Bariteau L, Djalalova IV, Myers T, Pezoa S, Turner DD, Wilczak JM. Sensitivity of thermodynamic profiles retrieved from ground-based microwave and infrared observations to additional input data from active remote sensing instruments and numerical weather prediction models. *Atmos Meas Tech*. 2024;17(13):3933–3948.
4. Illingworth AJ, Cimini D, Gaffard C, Haeffelin M, Lehmann V, Löhnert U, O'Connor EJ, Ruffieux D. Exploiting existing ground-based remote sensing networks to improve high-resolution weather forecasts. *Bull Am Meteorol Soc*. 2015;96(12):2107–2125.
5. Vural J, Merker C, Löffler M, Leuenberger D, Schraff C, Stiller O, Schomburg A, Knist C, Haefele A, Hervo M. Improving the representation of the atmospheric boundary layer by direct assimilation of ground-based microwave radiometer observations. *Q J R Meteorol Soc*. 2024;150(759):1012–1028.
6. Renju R, Raju CS, Swathi R, Milan VG. Retrieval of atmospheric temperature and humidity profiles over a tropical coastal station from ground-based microwave radiometer using deep learning technique. *J Atmos Solar Terr Phys*. 2023;249:106094.
7. Zhao H, Zeng Y, Hofste JG, Duan T, Wen J, Su ZB. Modeling of multi-frequency microwave backscatter and emission of land surface by a community land active passive microwave radiative transfer modeling platform. *J Remote Sens*. 2025;5:0415.
8. Xu G. A review of remote sensing of atmospheric profiles and cloud properties by ground-based microwave radiometers in central China. *Remote Sens*. 2024;16(6):966.
9. Chen J, Lv H, Wang Q, Wang G, Jia K, Zhao C, Shi W, Yan X. Revolutionizing satellite real-time air pollution alerts through new on-orbit system-on-chip technology. *Environ Sci Technol*. 2025.
10. World Meteorological Organization (WMO). *Guide to instruments and methods of observation (CIMO guide). WMO-No. 8*. Geneva (Switzerland): WMO; 2023.
11. Liljegren JC, Boukabara SA, Cady-Pereira K, Clough SA. The effect of the half-width of the 22-GHz water vapor line on retrievals of temperature and water vapor profiles with a 12-channel microwave radiometer. *IEEE Trans Geosci Remote Sens*. 2005;43(5):1102–1108.
12. Ricaud P, Genthon C, Durand P, Attié JL, Carminati F, Canut G, Vanacker JF, Moggio L, Courcoux Y, Pellegrini A, et al. Summer to winter diurnal variabilities of temperature and water vapour in the lowermost troposphere as observed by HAMSTRAD over dome C, Antarctica. *Bound Layer Meteorol*. 2012;143(1):227–259.
13. Cadeddu MP, Liljegren JC, Turner DD. The atmospheric radiation measurement (ARM) program network of microwave radiometers: Instrumentation, data, and retrievals. *Atmos Meas Tech*. 2013;6(9):2359–2372.
14. Temimi M, Fonseca RM, Nelli NR, Valappil VK, Weston MJ, Thota MS, Wehbe Y, Yousef L. On the analysis of ground-based microwave radiometer data during fog conditions. *Atmos Res*. 2020;231:104652.
15. International Telecommunication Union (ITU). *Use of radio spectrum for meteorology: Weather, water and climate monitoring and prediction*. Geneva (Switzerland): ITU; 2017.
16. Shrestha B, Brotzge JA, Wang J, Bain N, Thorncroft CD, Joseph E, Freedman J, Perez S. Overview and applications of the New York State Mesonet Profiler Network. *J Appl Meteorol Clim*. 2021;60(11):1591–1611.
17. Cimini D, Haeffelin M, Kotthaus S, Löhnert U, Martinet P, O'Connor E, Walden C, Coen MC, Preissler J. Towards the profiling of the atmospheric boundary layer at European scale-introducing the COST Action PROBE. *Bull Atmos Sci Technol*. 2020;1(1):23–42.
18. Rüfenacht R, Haefele A, Pospichal B, Cimini D, Bircher-Adrot S, Turp M, Sugier J. EUMETNET opens to microwave radiometers for operational thermodynamical profiling in Europe. *Bull Atmos Sci Technol*. 2021;2(1):4.
19. Rose T, Crewell S, Löhnert U, Simmer C. A network suitable microwave radiometer for operational monitoring of the cloudy atmosphere. *Atmos Res*. 2005;75(3):183–200.
20. Park MS, Park SH, Chae JH, Choi MH, Song Y, Kang M, Roh JW. High-resolution urban observation network for user-specific meteorological information service in the Seoul Metropolitan Area, South Korea. *Atmos Meas Tech*. 2017;10(4):1575–1594.
21. Che Y, Ma S, Xing F, Li S, Dai Y. An improvement of the retrieval of temperature and relative humidity profiles from a combination of active and passive remote sensing. *Meteorol Atmos Phys*. 2019;131(3):681–695.
22. Djalalova IV, Turner DD, Bianco L, Wilczak JM, Duncan J, Adler B, Gottas D. Improving thermodynamic profile retrievals from microwave radiometers by including radio acoustic sounding system (RASS) observations. *Atmos Meas Tech*. 2022;15(2):521–537.
23. Maahn M, Turner DD, Löhnert U, Posselt DJ, Ebell K, Mace GG, Comstock JM. Optimal estimation retrievals and their uncertainties: What every atmospheric scientist should know. *Bull Am Meteorol Soc*. 2020;101(9):E1512–E1523.
24. Adler B, Turner DD, Bianco L, Djalalova IV, Myers T, Wilczak JM. Improving solution availability and temporal consistency of an optimal estimation physical retrieval for ground-based thermodynamic boundary layer profiling. *Atmos Meas Tech*. 2024;17(22):6603–6624.
25. Walbröl A, Crewell S, Engelmann R, Orlandi E, Griesche H, Radenz M, Hofer J, Althausen D, Maturilli M, Ebell K. Atmospheric temperature, water vapour and liquid water path from two microwave radiometers during MOSAiC. *Sci Data*. 2022;9(1):534.

26. Yan X, Liang C, Jiang Y, Luo N, Zang Z, Li Z. A deep learning approach to improve the retrieval of temperature and humidity profiles from a ground-based microwave radiometer. *IEEE Trans Geosci Remote Sens*. 2020;58(12):8427–8437.
27. Cimini D, Rosenkranz PW, Tretyakov MY, Koshelev MA, Romano F. Uncertainty of atmospheric microwave absorption model: Impact on ground-based radiometer simulations and retrievals. *Atmos Chem Phys*. 2018;18(20):15231–15259.
28. Jiang S, Ma Y, Deng F, Lei L. A deep learning framework for enhanced retrieval of atmospheric temperature and humidity profiles across China: Unifying inversion algorithms across multiple stations. *Atmos Res*. 2025;315:107793.
29. Crewell S, Loehnert U. Accuracy of boundary layer temperature profiles retrieved with multifrequency multiangle microwave radiometry. *IEEE Trans Geosci Remote Sens*. 2007;45(7):2195–2201.
30. Seo J, Wagner TJ, Gero PJ, Turner DD. The impact of nonzenith elevation angles on ground-based infrared thermodynamic retrievals. *J Atmos Ocean Technol*. 2022;39(9):1395–1414.
31. LeCun Y, Bengio Y, Hinton G. Deep learning. *Nature*. 2015;521(7553):436–444.
32. Janiesch C, Zschech P, Heinrich K. Machine learning and deep learning. *Electron Mark*. 2021;31(3):685–695.
33. Zhu L, Bao Y, Lu Q, Fan S, Petropoulos GP, Mao J, Li Y, Li X. A method for retrieving thermodynamic atmospheric profiles using microwave radiometers of meteorological observation networks. *IEEE Trans Geosci Remote Sens*. 2022;60:4110311.
34. Luo Y, Wu H, Gu T, Wang Z, Yue H, Wu G, Zhu L, Pu D, Tang P, Jiang M. Machine learning model-based retrieval of temperature and relative humidity profiles measured by microwave radiometer. *Remote Sens*. 2023;15(15):3838.
35. Yu W, Xu X, Jin S, Ma Y, Liu B, Gong W. BP neural network retrieval for remote sensing atmospheric profile of ground-based microwave radiometer. *IEEE Geosci Remote Sens Lett*. 2022;19:4502105.
36. Xiao C, Dong J, Dou H, Li Y, Wang W, Ren F. A transformer network air temperature and humidity inversion method based on ATMS brightness temperature data. *IEEE Geosci Remote Sens Lett*. 2025;22:4500205.
37. Guo J, Miao Y, Zhang Y, Liu H, Li Z, Zhang W, He J, Lou M, Yan Y, Bian L. The climatology of planetary boundary layer height in China derived from radiosonde and reanalysis data. *Atmos Chem Phys*. 2016;16(20):13309–13319.
38. Yang Y, Ni C, Jiang M, Chen Q. Effects of aerosols on the atmospheric boundary layer temperature inversion over the Sichuan Basin, China. *Atmos Environ*. 2021;262:Article 118647.
39. Ding H, Liu L. Establishment and preliminary application of the forward modeling method for Doppler spectral density of ice particles. *Remote Sens*. 2020;12(20):3378.
40. Fang J, Huang K, Du M, Zhang Z, Cao R, Yi F. Investigation on cloud vertical structures based on Ka-band cloud radar observations at Wuhan in Central China. *Atmos Res*. 2023;281:106492.
41. Hersbach H, Bell B, Berrisford P, Hirahara S, Horányi A, Muñoz-Sabater J, Nicolas J, Peubey C, Radu R, Schepers D, et al. The ERA5 global reanalysis. *Q J R Meteorol Soc*. 2020;146(730):1999–2049.
42. Wang Y, Li Z, Wang Q, Jin X, Yan P, Cribb M, Li Y, Yuan C, Wu H, Wu T, et al. Enhancement of secondary aerosol formation by reduced anthropogenic emissions during Spring Festival 2019 and enlightenment for regional $PM_{2.5}$ control in Beijing. *Atmos. Chem Phys*. 2021;21(2):915–926.
43. Huang X, Wang Y, Shang Y, Song X, Zhang R, Wang Y, Li Z, Yang Y. Contrasting the effect of aerosol properties on the planetary boundary layer height in Beijing and Nanjing. *Atmos Environ*. 2023;308:119861.
44. Song X, Wang Y, Huang X, Wang Y, Li Z, Zhu B, Ren R, An J, Yan J, Zhang R, et al. The impacts of dust storms with different transport pathways on aerosol chemical compositions and optical hygroscopicity of fine particles in the Yangtze River Delta. *J Geophy Res Atmos*. 2023;128(24):Article e2023JD039679.
45. Massaro G, Stiperski I, Pospichal B, Rotach MW. Accuracy of retrieving temperature and humidity profiles by ground-based microwave radiometry in truly complex terrain. *Atmos Meas Tech*. 2015;8(8):3355–3367.
46. Zhou R, Wang G, Zhaxi S. Cloud vertical structure measurements from a ground-based cloud radar over the southeastern Tibetan Plateau. *Atmos Res*. 2021;258:105629.
47. Yan X, Zuo C, Li Z, Chen HW, Jiang Y, Wang Q, Wang G, Jia K, A Y, Chen Z, et al. Substantial underestimation of fine-mode aerosol loading from wildfires and its radiative effects in current satellite-based retrievals over the United States. *Environ Sci Technol*. 2024;58(35):15661–15671.
48. Lundberg SM, Lee SL. A unified approach to interpreting model predictions. Paper presented at: 31st Annual Conference on NIPS; 2017; New York, NY, USA.
49. Kang Y, Choi H, Im J, Park S, Shin M, Song CK, Kim S. Estimation of surface-level NO_2 and O_3 concentrations using TROPOMI data and machine learning over East Asia. *Environ Pollut*. 2021;288:117711.
50. Jiang M, Chen Z, Yang Y, Ni C, Yang Q. Establishment of aerosol optical depth dataset in the Sichuan Basin by the random forest approach. *Atmos Pollut Res*. 2022;13(5):101394.
51. Jung Y. Multiple predicting K-fold cross-validation for model selection. *J Nonparametr Stat*. 2018;30(1):197–215.
52. Ke GL, Meng Q, Finley T, Wang TF, Chen W, Ma WD, Ye QW, Liu TY. LightGBM: A highly efficient gradient boosting decision tree. Paper presented at: 31st Annual Conference on NIPS; 2017; New York, NY, USA.
53. Wen X, Xie Y, Wu L, Jiang L. Quantifying and comparing the effects of key risk factors on various types of roadway segment crashes with LightGBM and SHAP. *Accid Anal Prev*. 2021;159:106261.
54. Chen X, Ishwaran H. Random forests for genomic data analysis. *Genomics*. 2012;99(6):323–329.
55. Cimini D, Nelson M, Güldner J, Ware R. Forecast indices from a ground-based microwave radiometer for operational meteorology. *Atmos Meas Tech*. 2015;8(1):315–333.
56. Xu H, Guo J, Tong B, Zhang J, Chen T, Guo X, Zhang J, Chen W. Characterizing the near-global cloud vertical structures over land using high-resolution radiosonde measurements. *Atmos Chem Phys*. 2023;23(23):15011–15038.
57. Zhang L, Liu M, He W, Xia X, Yu H, Li S, Li J. Ground passive microwave remote sensing of atmospheric profiles using WRF simulations and machine learning techniques. *J Meteorol Res*. 2024;38(4):680–692.
58. Li W, Zhang F, Shi Y, Iwabuchi H, Zhu M, Li J, Han W, Letu H, Ishimoto H. Efficient radiative transfer model for thermal infrared brightness temperature simulation in cloudy atmospheres. *Opt Express*. 2020;28(18):25730–25749.
59. Wei X, Min M, Li J, Sun F, Qin D, Yao Z. Characteristics of strong storms at the pre-convection stage from satellite microwave sounder observations. *J Geophy Res Atmos*. 2022;127(22):Article e2022JD037216.

Journal of Remote Sensing
A SCIENCE PARTNER JOURNAL

Revolutionizing Clear-Sky Humidity Profile Retrieval with Multi-Angle-Aware Networks for Ground-Based Microwave Radiometers

Yinshan Yang, Zhanqing Li, Jianping Guo, Yuying Wang, Hao Wu, Yi Shang, Ye Wang, Langfeng Zhu, and Xing Yan

Citation: Yang Y, Li Z, Guo J, Wang Y, Wu H, Shang Y, Wang Y, Zhu L, Yan X. Revolutionizing Clear-Sky Humidity Profile Retrieval with Multi-Angle-Aware Networks for Ground-Based Microwave Radiometers. *J Remote Sens*. 2025;**5**:0736. DOI: 10.34133/remotesensing.0736

Accurate retrieval of atmospheric relative humidity (RH) profiles is essential for improving our understanding of atmospheric thermodynamics and climate change. Nevertheless, it remains challenging, as traditional models rely exclusively on vertical brightness temperature (BT) observations. Here, we present a novel retrieval algorithm called AngleNet, a groundbreaking deep-learning model that leverages multi-angle BT observation from ground-based microwave radiometers (MWRs). The innovative "multi-angle-aware" module in AngleNet effectively exploits previously underutilized oblique scanning angle data by accurately capturing these nonlinear relationships between BT and RH profiles, and precisely characterizes its vertical fine structure. Based on the 7-year (2018–2024) in situ measurements from Beijing, Nanjing, and Shanghai, validation results reveal that AngleNet achieves substantial improvements, with an average $R2$ of 0.71 and a root mean square error (RMSE) of 10.39%, surpassing conventional models such as LGBM (light gradient boosting machine) and RF (random forest) by over 10% in both metrics, and demonstrating a remarkable 41% increase in $R2$ and a 10% reduction in RMSE compared to the previous BRNN method (batch normalization and robust neural network). Moreover, additional independent validation results demonstrate that AngleNet exhibits excellent stability and retrieval accuracy during periods without radiosonde measurements. Feature analysis and evaluations of the "multi-angle-aware" module indicate that optimal RH retrieval performance is achieved by combining zenith-angle BTs with oblique angles at 30° and 19.2°. AngleNet breakthrough performance is especially notable in consistently capturing complex RH profile features, which are critical for accurate numerical weather forecasting and climate monitoring.
Image

Journal of Remote Sensing (ISSN 2694-1589) is published by the American Association for the Advancement of Science. 1200 New York Avenue NW, Washington, DC 20005.